Supplemental Information

Regulating location of active sites: A Novel Strategy to Greatly Improve Stability of PtAu Electrocatalysts

Suying Xu,[†a] Wenjie Hou,[†a] Rui Jiang,[a] Li Li, [a] Tian Sheng,*[b] and Leyu Wang*[a]

[a]State Key Laboratory of Chemical Resource Engineering, Beijing Advanced Innovation Center for Soft Matter Science and Engineering, Beijing University of Chemical Technology, Beijing 100029, China

[b]College of Chemistry and Materials Science, Anhui Normal University, Wuhu, 241000, Anhui, China

Contents

1. Supplemental Figures and Tables

Table S1. List of compositions of the bulk, surface as well as feeding ratios of PtAu alloys.

Designation	feeding ratio of Pt/Au in precursor	As synthesized NCs (ICP-OES)	As synthesized NCs (XPS)
$Pt_{46}Au_{54}$	50:50	46:54	61:39
$Pt_{24}Au_{76}$	25:75	24:76	47:53
$Pt_{14}Au_{86}$	17:83	14:86	30:70

As evidenced by ICP-OES results (Figure 1e and Table S1), the resulting molar ratios of Pt and Au were similar to that of feeding ratios, namely, $Pt_{46}Au_{54}$, $Pt_{24}Au_{76}$ and $Pt_{14}Au_{86}$ corresponding closely to 1:1, 1:3, and 1:5, respectively. Whereas, the surface composition obtained from XPS results revealed an obvious deviation from that obtained by ICP-OES, that is, the molar ratios of Pt/Au were 6:4, 5:5 and 3:7, for $Pt_{46}Au_{54}$, $Pt_{24}Au_{76}$ and $Pt_{14}Au_{86}$, respectively.

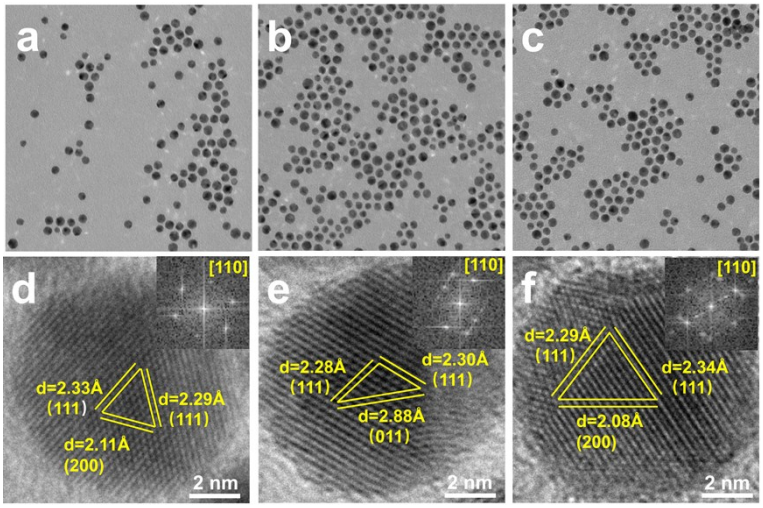

Figure S1. TEM and HRTEM characterization. TEM (a-c) and HRTEM (d-f) images and corresponding fast Fourier transform (FFT) patterns of PtAu alloys with feeding Pt/Au ratios of (a, d) 1:1, (b, e) 1:3, and (c, f) 1:5, respectively. The fast Fourier transform (FFT) patterns suggest that all the PtAu alloys are single crystalline as viewed from the zone axis of [110].

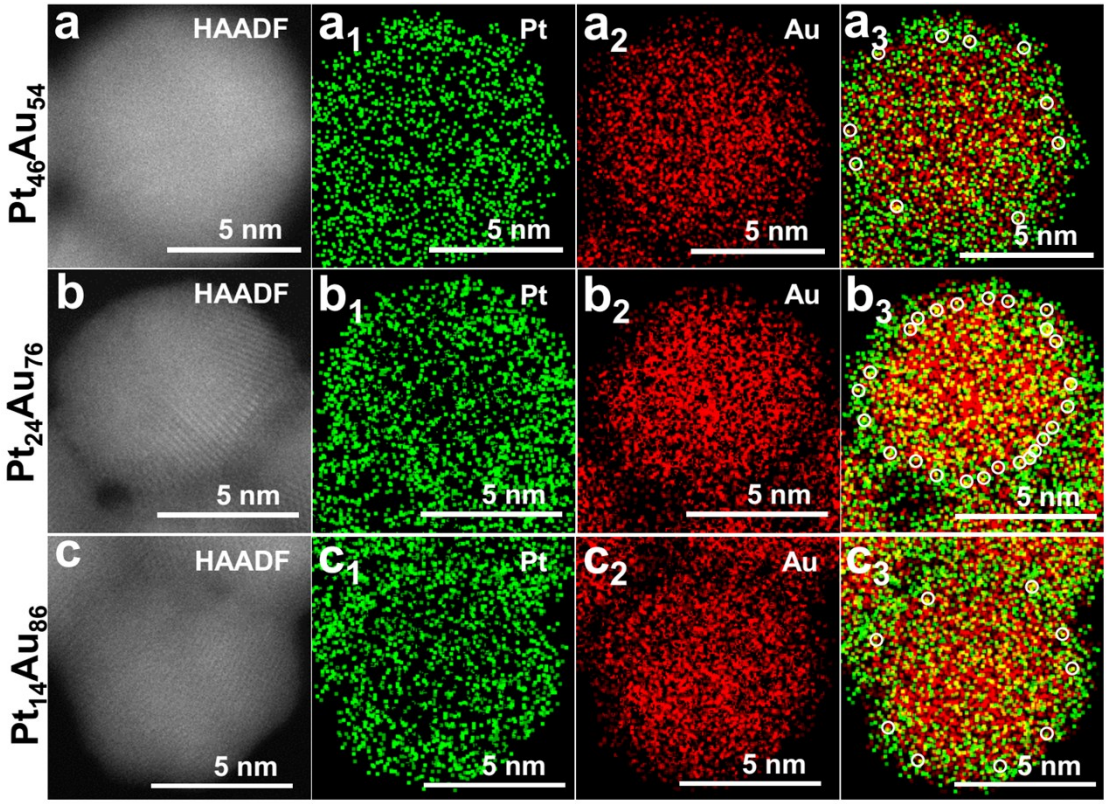

Figure S2. Atomic-resolution aberration-corrected HAADF-STEM and EDS elemental mapping characterization. Atomic-resolution aberration-corrected HAADF-STEM images (a, b, c) and elemental mapping images (a_1-a_3, b_1-b_3 and c_1-c_3) belong to $Pt_{46}Au_{54}$, $Pt_{24}Au_{76}$ and $Pt_{14}Au_{86}$, respectively. Note that it is very challenging to exactly map out the location of Pt and Au atoms even with atomic resolution HAADF-STEM and elemental mapping. Here, the green and red colors represent Pt and Au elements, respectively and the yellow pixel means areas are both in presence of Pt and Au. Judging from image a_3, b_3 and c_3, clearly, there are much more yellow pixels (highlighted with circles) at the edge of $Pt_{24}Au_{76}$ nanoparticles than that in $Pt_{46}Au_{54}$ and $Pt_{14}Au_{86}$, which suggests that Pt and Au located with closer distance at the surface of $Pt_{24}Au_{76}$ alloy.

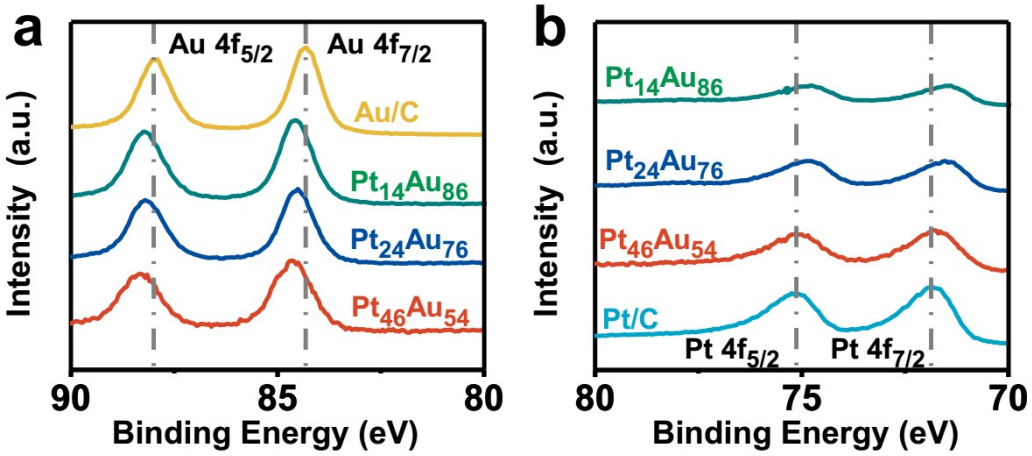

Figure S3. XPS patterns. Au (a) and Pt (b) 4f region of XPS patterns of PtAu NPs and commercial Pt/C, related to Figure 1.

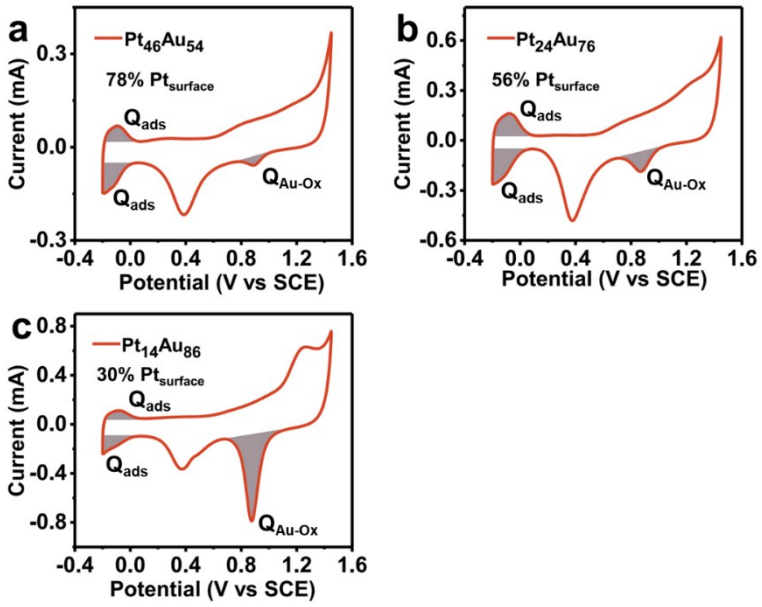

Figure S4. ESA measurements. Cyclic voltammograms of $Pt_{46}Au_{54}$ (a), $Pt_{24}Au_{76}$ (b) and $Pt_{14}Au_{86}$ (c) nanocrystals in 0.5 M H_2SO_4 at 50 mV/s, related to Figure 1. The Pt and Au surface composition were calculated through charges associated with integration of hydrogen adsorption/desorption and Au oxide reduction area. The surface Pt contents obtained *via* cyclic voltammetry curves (Figure S4) were 78%, 56%, and 30% for $Pt_{46}Au_{54}$ (61% in XPS, Table S1), $Pt_{24}Au_{76}$ (47% in XPS, Table S1) and $Pt_{14}Au_{86}$ (30% in XPS, Table S1), respectively. All the results indicate that the surface Pt/Au ratio is higher than that of bulk nanocatalysts.

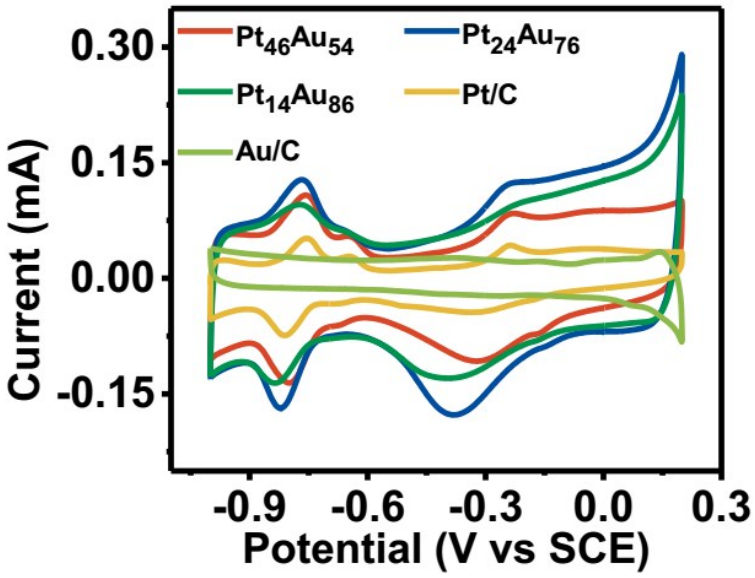

Figure S5. ECSA tests. CV curves of $Pt_{46}Au_{54}$, $Pt_{24}Au_{76}$, $Pt_{14}Au_{86}$, commercial Pt/C and Au/C with potential ranging from -1.0 to 0.2 V (*vs* SCE) in 1.0 M KOH solution at a scan rate of 50 mV s^{-1}, related to Figure 2. The onset potential of Pt-oxides in $Pt_{24}Au_{76}$ is lower than its counterparts in the absence of methanol (Figure S5), implying $Pt_{24}Au_{76}$ could provide hydroxyl species at lower potentials. The corresponding ECSA values were determined by integrating the hydrogen adsorption peak area in the forward potential scan after correction for the double-layer charging current. The area of the Pt-oxides of $Pt_{24}Au_{76}$ was much larger than others, which revealed that $Pt_{24}Au_{76}$ can provide much more OH* to oxidize CO-like intermediates adsorbed on the surface of Pt active sites in methanol oxidation process. Here, the ECSA values for $Pt_{46}Au_{54}$, $Pt_{24}Au_{76}$ and $Pt_{14}Au_{86}$ and Pt/C are 80 m^2/g_{Pt}, 83.1 m^2/g_{Pt}, 56.7 m^2/g_{Pt}, 37.1 m^2/g_{Pt}, respectively (Figure 2c, left part), whereas Au/C were electrochemically inert as evidenced by the negligible activity and ECSA value, which indicated that incorporating Au element would increase exposure of Pt element, leading to increase of effective surface Pt sites.

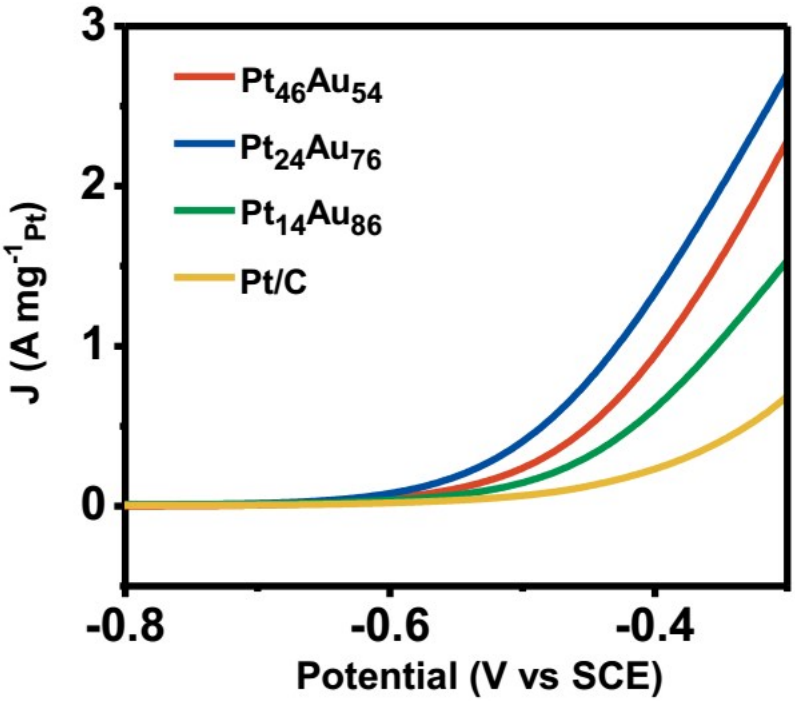

Figure S6. Onset potential tests. The onset potentials of PtAu alloys in 1.0 M methanol and 1.0 M KOH solution at a scan rate of 50 mV s^{-1}, related to Figure 2. The onset potentials are -0.650 V, –0.621 V, –0.606 V and –0.558 V for $Pt_{24}Au_{76}$, $Pt_{46}Au_{54}$, $Pt_{14}Au_{86}$ and Pt/C, respectively.

Table S2. Comparison of electrocatalytic performance of PtAu alloys and Pt/C with regard to MOR.

Catalyst	**ECSA ($m^2/g_{Pt/Pd}$)**	**J_s (mA/cm^2_{Pt})**	**J_m (A/mg_{Pt}) (Initial)**	**J_m (A/mg_{Pt}) (After 10000s)**
$Pt_{46}Au_{54}$	80.0	5.44	4.31	0.03
$Pt_{24}Au_{76}$	83.1	5.61	4.66	2.23
$Pt_{14}Au_{86}$	56.7	4.72	2.65	0.33
Pt/C	37.1	3.09	1.14	0.01

Table S3. Comparison of electrocatalytic activity with previously reported Pt or Pd-based catalysts with regard to MOR.

Catalyst	Electrolyte solution	[a]J_m	[b]J_s	ECSA ($m^2/g_{Pt/Pd}$)	Reference
PtCu NFs	0.5 M KOH + 1 M CH_3OH	2260	18.2	12.4	*Adv. Mater.,* **2016**, 28, 8712–8717
Pt-$Ni(OH)_2$–graphene	1.0 M KOH + 1.0 M CH_3OH	1236	--	64.1	*Nat. Commun.,* **2015**, 6,10035.
Pd_3Pb NSAs/C	1.0 M KOH + 1.0 M CH_3OH	2980	4.41	67.5	*ACS Catal.*, **2018**, 8, 4569−4575
Pt−Pd−Cu nanodendrites	0.1 M KOH + 0.5 M CH_3OH	1447	--	39.3	*ACS Appl. Mater. Interfaces*, **2017**, 9, 44018−44026
$Pd_{45}Pt_{55}$	1.0 M KOH + 1.0 M CH_3OH	~2000	--	--	*Adv. Mater.*, **2012**, 24, 2326–2331
Au/PtCu nanowires	1.0 M KOH + 1.0 M CH_3OH	~2000	--	--	*Small*, **2014**, 10, No. 16, 3262–3265
PtZn/MWNT-E	0.1 M KOH + 0.5 M CH_3OH	~550	~1.15	--	*J. Am. Chem. Soc.*, **2017**, 139, 4762−4768
ITO/SSG/$M_{13}Y_3E$/rGO/($Au_{58.9}$−$Pt_{41.1}$)	0.1 M KOH + 0.1 M CH_3OH	1542.8	--	153.23	*ACS Appl. Mater. Interfaces*, **2017**, 9, 32965−32976
Dealloyed-CoAuPd	1.0 M KOH + 1.0 M CH_3OH	495.85	1.16	42.64	*ACS Appl. Energy Mater.*, **2018**, 1, 2619−2629
$Pt_{3.5}Pb$ NNWs	0.5 M KOH + 1 M CH_3OH	2840	6.51	42.2	*Nanoscale*, **2017**, 9, 201–207
$Pt_{(CuCl)1}$/Au/GCE	0.5 M KOH + 1 M CH_3OH	23700	--	--	*Chem. Commun.*, **2018**, 54, 3743
rGO–Au@Pt NPs	0.5 M KOH + 0.5 M CH_3OH	6245	2.76	226.15	*J. Mater. Chem. A*, **2015**, 3, 18010
$Pt_{24}Pd_{26}Au_{50}$/Ppy	0.1 M KOH + 1 M CH_3OH	12500	6.76	265	*Sustain. Energy Fuels*, **2017**, 1, 1148
PdCu alloy microparticles	1.0 M KOH + 1.0 M CH_3OH	1462	3.32	44.15	*ACS Appl. Energy Mater.*, **2018**, 1, 3323−3330

$Pd_{10}Ag_{10}$/CNT	1 M KOH + 0.5 M CH_3OH	731	27	46	*ACS Appl. Energy Mater.*, **2018**, 1 (8), pp 3763–3770
$Pd_{45.5}Pt_{54.5}$	1 M KOH + 0.5 M CH_3OH	5260	--	--	*Nanoscale*, **2016**, 8, 14705–14710
Pd@PtNi NSs	1.0 M KOH + 1.0 M CH_3OH	1614.3	2.68	59.5	*ACS Appl. Nano Mater.*, **2018**, 1, 3226−3235
PtPdNi 3DNA	1.0 M KOH + 1.0 M CH_3OH	4950	--	23.34	*ACS Appl. Energy Mater.,* **2018**, 1, 32−37
p-Pt_1Cu_1/AP-GNPs	0.1 M KOH + 0.5 M CH_3OH	3610	--	91.89	*J. Mater. Chem. A*, **2016**, 4, 3316
Au@Pt PNPs	0.1 M KOH + 0.5 M CH_3OH	5004	26.05	--	*ACS Appl. Mater. Interfaces*, **2017**, 9, 32688−32697
Pd/Co-CeO_2	1 M KOH + 0.5 M CH_3OH	2418.5	--	48.9	*Nanoscale*, **2017**, 9, 12565
$Pd_{30}Au_{70}$/C	1.0 M KOH + 1.0 M CH_3OH	950.6	--	--	*J. Mater. Chem. A*, **2013**, 1, 9157
$CuPt_1Au_3$	1.0 M KOH + 1.0 M CH_3OH	1959.67	--	24.77	*Electrochimica Acta*, **2018**, 282,792-798
AgAu@Pt nanoframes	0.2 M KOH + 1 M CH_3OH	483.1	1.96	24.6	*Nanoscale*, **2018**, 10, 2231
Pd_1Ru_1 NFs	1.0 M KOH + 1.0 M CH_3OH	1280.2	4.9	30.2	*J. Colloid Interface Sci.*, **2017**, 505, 1–8
20 wt% PtRu/C	1.0 M KOH + 1.0 M CH_3OH	~600	--	--	*Nat. Commun.,* **2015**, 6,10035
PtRu/RGO/GC	1.0 M KOH + 1.0 M CH_3OH	~398.9	--	--	*J. Mater. Chem. A*, **2013**, 1, 7255-7261
commercial PtRu	1.0 M KOH + 0.5 M CH_3OH	611.3	--	--	*Nanoscale*, **2017**, 9, 12565
$Pt_{24}Au_{76}$ NPs	**1.0 M KOH + 1.0 M CH_3OH**	**4660**	**5.61**	**83.1**	**This work**

[a] The unit for J_m is $mA/mg_{Pt/Pd}$.

[b] The unit for J_s is $mA/cm^2_{Pt/Pd}$.

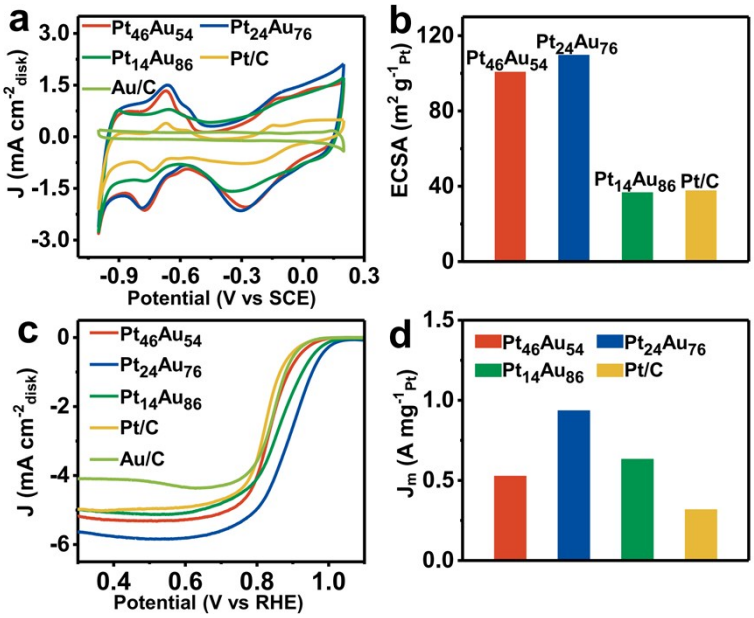

Figure S7. Electrochemical tests of ORR. (a) CV curves of PtAu alloys, Au/C and commercial Pt/C in 0.1 M KOH solution at a scan rate of 50 mV s^{-1}, related to Figure 2. (b) ECSA values of PtAu alloys and commercial Pt/C. (c) ORR polarization curves of PtAu alloys, Au/C and commercial Pt/C in 0.1 M KOH solution. (d) The histogram of mass activities of PtAu alloys and commercial Pt/C at 0.8 V vs RHE. Cyclic voltammetries of PtAu alloys (Figure S7a) were first conducted as compared with that of benchmark Pt/C and Au/C. Remarkably, the onset potential for hydroxyl oxidation shifted from –0.31 V to –0.40 V (*vs* SCE) in comparison with that of Pt/C, suggesting a stronger oxygen binding energy on the surface of PtAu alloys, which would enhance the adsorptive capacity to O_2 and promote ORR activity. The ECSA for each catalyst was calculated through integrating hydrogen desorption peak recorded in the CV curve (Figure S7b), and the ECSA of $Pt_{24}Au_{76}$ was 110 m^2/g_{Pt}, 2.9 times that of Pt/C (38 m^2/g_{Pt}), implying that bimetallic PtAu structure could effectively expose more valid reactive sites. Figure S7c displayed the polarization curves of different catalysts for ORR acquired on a rotating disk electrode (RDE) in 0.1 M KOH solution at 1,600 rpm. Specific half-wave potential, onset potential values were listed in Table S4. The $Pt_{24}Au_{76}$ possessed the highest mass activity (J_m) of 0.934 A/mg_{Pt} (at 0.8 V *vs* RHE), which is 2.9 times that of commercial Pt/C catalyst (Figure S7d).

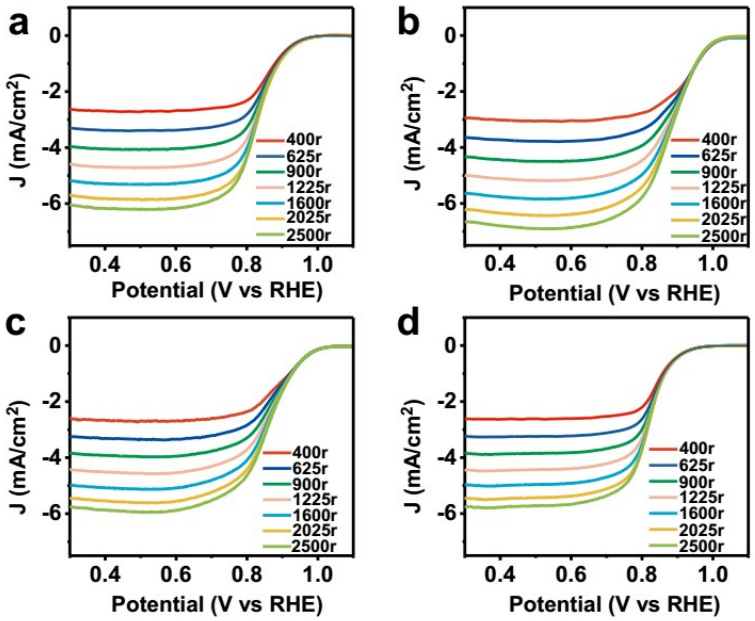

Figure S8. Linear sweep voltammograms curves at different rotating rates. Rotating disk electrode linear sweep voltammograms obtained for (a) $Pt_{46}Au_{54}$, (b) $Pt_{24}Au_{76}$, (c) $Pt_{14}Au_{86}$ and (d) Pt/C NPs at various scanning rates, related to Figure 2.

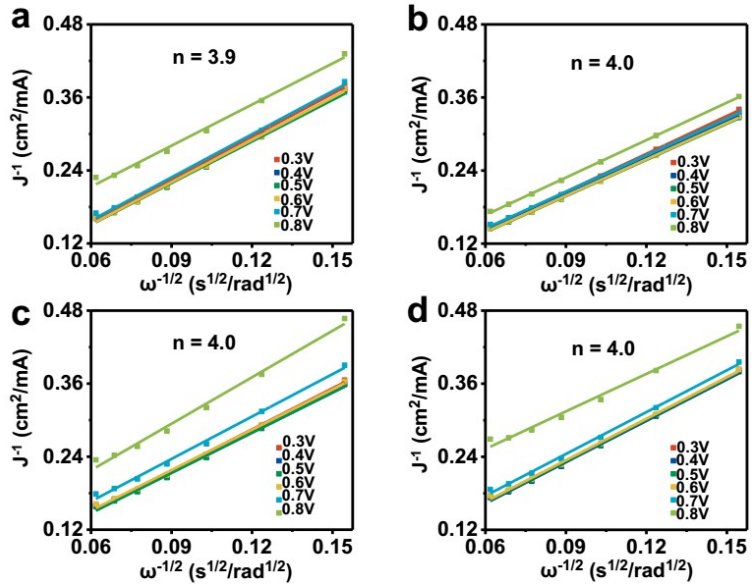

Figure S9. Koutecky-Levich plots. Koutecky-Levich plots for of (a) $Pt_{46}Au_{54}$, (b) $Pt_{24}Au_{76}$, (c) $Pt_{14}Au_{86}$ and (d) Pt/C, respectively, related to Figure 2. The transferred electron number per oxygen molecule in the ORR was calculated and listed accordingly. In order to obtain more information about the electron-transfer process of the catalysts, linear sweep voltammograms at different rotating rates of rotating disk electrode (RDE) were noted (Figure S8). The Koutecky-Levich plots gained from the LSV curves were shown in Figure S9, which proved that all PtAu alloys had similar electron transfer numbers ($n \approx 4.0$) to that of commercial Pt/C at various potentials.

Table S4. The list of relational data of PtAu alloys and commercial Pt/C for ORR in 0.1 M KOH.

Catalyst	Onset potential (V *vs* RHE)	Limiting current density (mA/cm^2)	$E_{1/2}$ (V *vs* RHE)	ECSA (m^2/g_{Pt})	Mass activity at 0.8 V vs RHE (A/mg_{Pt})
$Pt_{46}Au_{54}$	0.99	5.2	0.838	101	0.527
$Pt_{24}Au_{76}$	1.04	5.7	0.896	110	0.934
$Pt_{14}Au_{86}$	1.01	5.0	0.866	37	0.633
Pt/C	0.97	5.0	0.824	38	0.318

Table S5. Comparison of durability of previously reported Pt or Pd-based catalysts with regard to MOR.

Catalyst	Electrolyte solution	*I-t* potential (V)	Duration (s)	$J_{Initial}$ ($mA/mg_{Pt\ or\ Pd}$)	J_{Final} ($mA/mg_{Pt\ or\ Pd}$)	Reference
AgAu@Pt nanoframes	0.2 M KOH + 1 M CH_3OH	-0.3 (Ag/AgCl)	1500	~300	~162	*Nanoscale*, **2018**, 10, 2231–2235
$Pt/Ni(OH)_2/rGO$	1 M KOH + 1 M CH_3OH	-0.3 (SCE)	3600	~650	>460	*Nat. Commun*. **2015**, 6: 10035
PtCu NFs	0.5 M KOH + 1 M CH_3OH	-0.7 (RHE)	3000	~1500	~500	*Adv. Mater*. **2016**, 28, 8712–8717
$Pd_{45}Pt_{55}$	1 M KOH + 1 M CH_3OH	-0.2 (Ag/AgCl)	200	1300	<800	*Adv. Mater.* **2012**, 24, 2326–2331
Au/PtCu nanowires	1 M KOH + 1 M CH_3OH	-0.15 (Ag/AgCl)	4000	~1300	~250	*Small*, **2014**, 10, 16, 3262–3265
PtZn/MWNT-E	0.1 M KOH + 0.5 M CH_3OH	-0.1 (Ag/AgCl)	900	~550	~200	*J. Am. Chem. Soc.* **2017**, 139, 4762−4768
$Pd/Co\text{-}CeO_2$	1 M KOH + 0.5 M CH_3OH	-0.3 (Hg/HgO)	10800	~650	<100	*Nanoscale*, **2017**, 9, 12565–12572
$Pt_{(CuCl)1}/Au/GCE$	0.5 M KOH + 1 M CH_3OH	-0.3 (SCE)	1200	~6500	<750	*Chem. Commun.*, **2018**, 54, 3743
$Pt_{24}Pd_{26}Au_{50}/Ppy$	0.1 M KOH + 1 M CH_3OH	-0.1 (Ag/AgCl)	3600	~13250	~1325	*Sustain. Energy Fuels*,**2017**, 1, 1148
rGO–Au@Pt NPs	0.5 M KOH + 0.5 M CH_3OH	-0.46 (Ag/AgCl)	1000	~400	~80	*J. Mater. Chem. A*, **2015**, 3,18010
Bowl-like PdCu alloy hollow microparticles	1 M KOH + 1 M CH_3OH	-0.2 (Ag/AgCl)	4000	300	50	*ACS Appl. Energy Mater*. **2018**, 1, 3323−3330
$Pd_{10}Ag_{10}/CNT$	1 M KOH + 0.5 M CH_3OH	−0.2 V (Hg/HgO)	200	300	~115	*ACS Appl. Energy Mater.*, **2018**, 1, 3763–3770

$Pd_{45.5}Pt_{54.5}$	1 M KOH + 0.5 M CH_3OH	-0.2 (Ag/AgCl)	3600	~3300	370	*Nanoscale*, **2016**, 8, 14705–14710
Pd@PtNi NSs	1 M KOH + 1 M CH_3OH	0.9 （RHE）	10000	~1300	~500	*ACS Appl. Nano Mater.*, **2018**, 1, 3226−3235
PtPdNi 3DNA	1 M KOH + 1 M CH_3OH	-0.25 (Ag/AgCl)	10000	~1900	1300	*ACS Appl. Energy Mater.* **2018**, 1, 32−37
p-Pt_1Cu_1/AP-GNPs	0.1 M KOH + 0.5 M CH_3OH	-0.3 (SCE)	7200	~2900	~900	*J. Mater. Chem. A*, **2016**, 4, 3316
Au@Pt PNPs	0.1 M KOH + 0.5 M CH_3OH	0.2 (Ag/AgCl)	800	~5700	1920	*ACS Appl. Mater. Interfaces* **2017**, 9, 32688−32697
$Pd_{30}Au_{70}$/C	1 M KOH + 1 M CH_3OH	−0.2 V (Hg/HgO)	1000	500	~200	*J. Mater. Chem. A*, **2013**, 1, 9157
$CuPt_1Au_3$	1 M KOH + 1 M CH_3OH	-0.205 (Ag/AgCl)	1000	2000	~100	*Electrochimica Acta*,**2018**, 282,792-798
AgAu@Pt nanoframes	0.2 M KOH + 1 M CH_3OH	-0.3 (Ag/AgCl)	1500	~300	~160	*Nanoscale*, **2018**, 10, 2231
Pd_1Ru_1 NFs	1 M KOH + 1 M CH_3OH	-0.4 (SCE)	3600	<1300	~200	*J. Colloid Interface Sci.,*2017,505,1–8
20 wt% PtRu/C	1 M KOH + 1 M CH_3OH	-0.3 (SCE)	3600	~600	~200	*Nat. Commun.,* **2015**, 6,10035
PtRu/RGO/GC	1.0 M KOH + 1.0 M CH_3OH	-0.3 (SCE)	4000	~400	<50	*J. Mater. Chem. A*, **2013**, 1, 7255-7261
commercial PtRu	1.0 M KOH + 0.5 M CH_3OH	-0.2 (Hg/HgO)	10800	~500	30.1	*Nanoscale*, **2017**, 9, 12565-12572
$Pt_{24}Au_{76}$	**1 M KOH + 1 M CH_3OH**	**-0.1 (SCE)**	**10,000**	**4660**	**2230**	**This work**

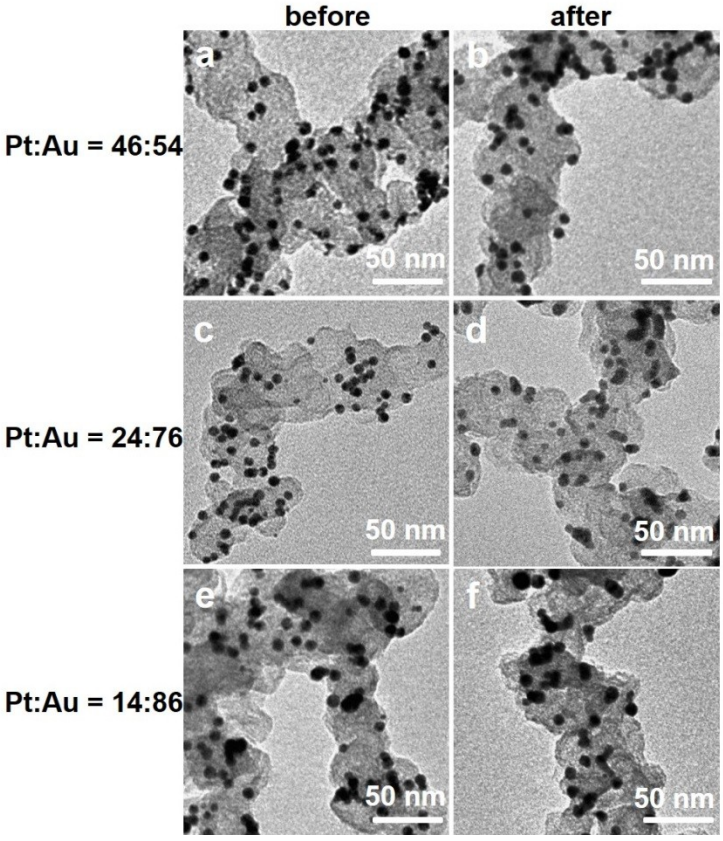

Figure S10 TEM images of PtAu alloys before (a, c, e) and after (b, d, f) chronoamperometric tests (10000 s).

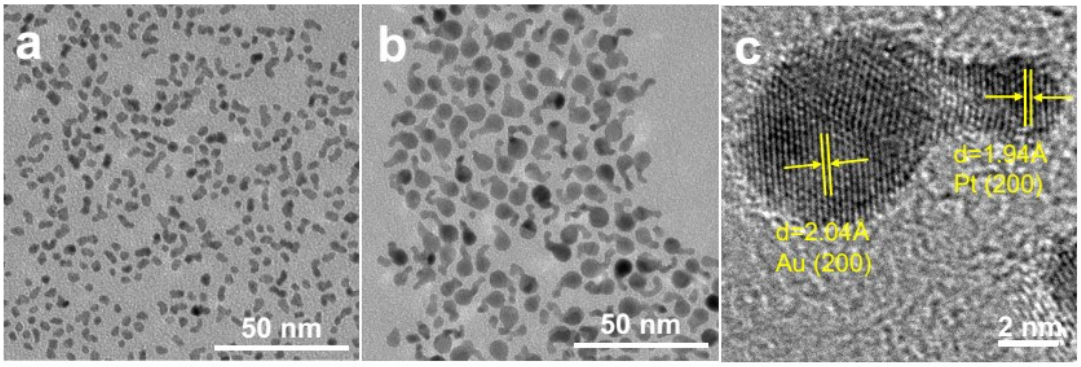

Figure S11. TEM characterization. TEM images of (a) Pt nanocrystals prepared at 230 °C, (b) Pt/Au heterodimer and (c) HRTEM image of Pt/Au heterodimer, related to Figure 2.

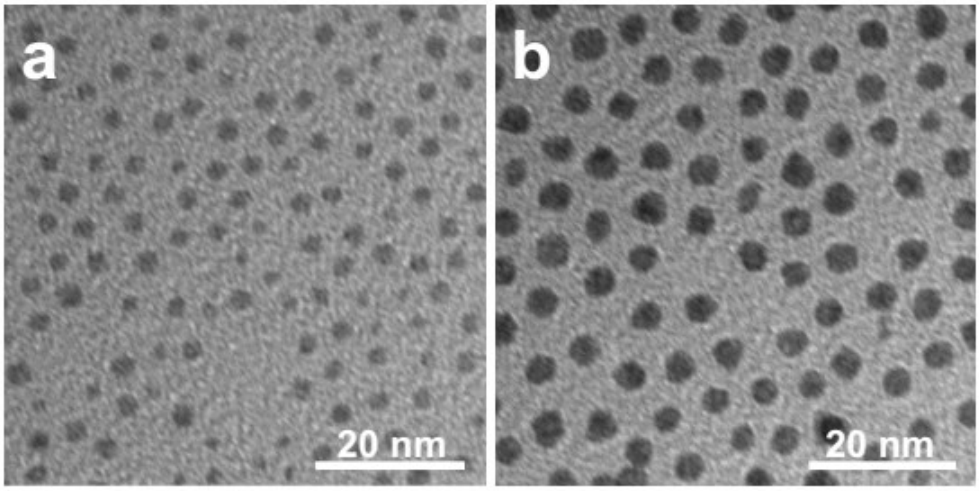

Figure S12. TEM characterization. TEM images of (a) Au seeds reduced by TBAB and (b) Au@Pt nanostructure, related to Figure 2.

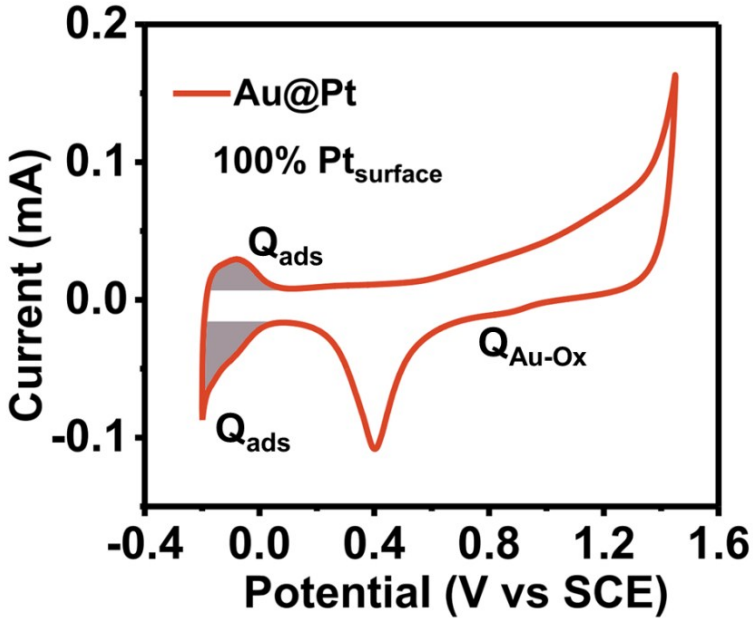

Figure S13. ESA measurement. Cyclic voltammograms of Au@Pt core/shell nanostructure in 0.5 M H_2SO_4 at 50 mV/s, related to Figure 2.The Pt and Au surface composition were calculated, through the charges associated with integration of hydrogen adsorption/desorption and Au oxide reduction area. Judging from Figure S12, clearly, there is no Au oxide reduction peak, implying the absence of Au element on the surface. The surface Pt contents obtained and calculated to be 100%.

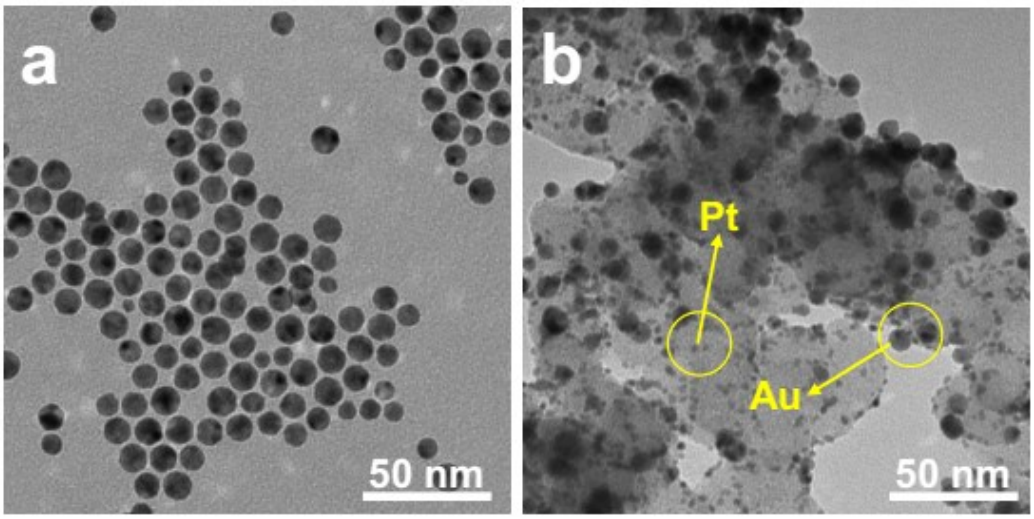

Figure S14. TEM characterization. TEM images of (a) Au NPs synthesized at 180 °C and (b) mixture of Au and Pt (Au + Pt), related to Figure 2.

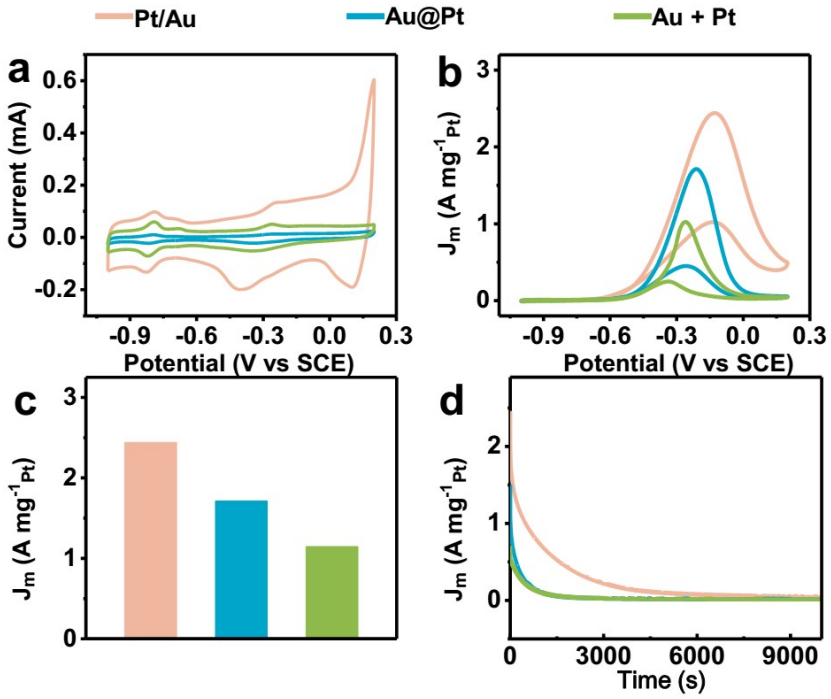

Figure S15. Electrochemical measurements of contrast samples for MOR. (a) CV curves of Pt/Au heterodimer, Au@Pt core-shell nanostructure and Au + Pt in 1.0 M KOH solution at a scan rate of 50 mV s^{-1}, related to Figure 2. (b) CV curves of control samples including Pt/Au, Au@Pt, and Au + Pt in 1.0 M methanol and 1.0 M KOH solution at a scan rate of 50 mV s^{-1}. (c) The histogram of mass activities. (d) The chronoamperometric tests of Pt/Au, Au@Pt and Au + Pt in 1.0 M methanol and 1.0 M KOH solution at their own peak potential of -0.25V, -0.2V and -0.15V (*vs* SCE), respectively. All the control samples possess lower ECSA values (24.7 m^2/g_{Pt}, 14.2 m^2/g_{Pt} and 34.1 m^2/g_{Pt}) for Pt/Au, Au@Pt, and Au + Pt, respectively, obtained from Figure S14a. We assumed that thoroughly mixing of

Pt and Au atoms plays vital roles in increasing the ECSA values of the nanocatalysts. Their normalized mass activities are 2.44 A/mg_{Pt}, 1.71 A/mg_{Pt} and 1.15 A/mg_{Pt} for Pt/Au, Au@Pt, and Au + Pt, respectively, as depicted in Figure S14b-c, far lower than that acquired by PtAu alloys, which means that 100% coverage of Pt elements for Au@Pt displayed, however, lower catalytic efficiency than that of Pt/Au. Besides, their durability was far less satisfied. Au@Pt and physical mixture (Au + Pt) are almost inactive after 1,000 sec, as exhibited in Figure S14d. Though Pt/Au displayed a bit better stability, still it lost about 90% of its catalytic efficiency within 2,500 s. All these results implied the heterodimer Pt/Au displayed better catalytic efficiency than that of Au + Pt and Au@Pt nanostructures and we assumed partially formation of PtAu alloy would occur particularly at the junction site of Pt/Au heterodimer, which to some extent, implied that the proper arrangement of Au and Pt active sites impose dramatically effect on the catalytic performance. Thus, the formation of PtAu alloy would further improve the catalytic performance.

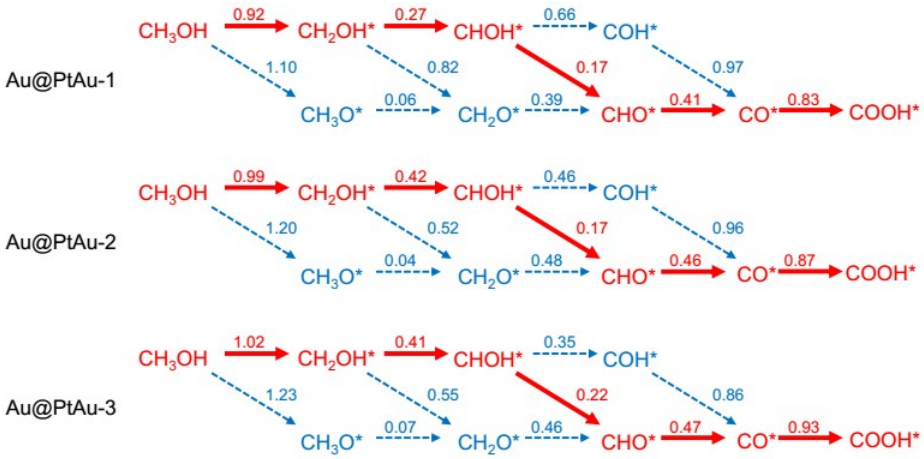

Figure S16. DFT calculation. Calculated kinetic barriers (in eV) for the elementary steps in methanol decomposition, related to Figure 3. The preferred reaction pathways were highlighted in red.

Table S6. Calculated activation energies (E_a) and reaction energies (ΔG) in eV of elementary steps on different surfaces, respectively, in methanol electro-oxidation under the condition of U = -0.4 V *vs* SCE, pH = 14.

Reactions	Au@PtAu-1		Au@PtAu-2		Au@PtAu-3	
	E_a	ΔG	E_a	ΔG	E_a	ΔG
$CH_3OH + OH^- \rightarrow CH_2OH^* + H_2O + e^-$	0.92	-0.17	0.99	-0.22	1.02	-0.25
$CH_3OH + OH^- \rightarrow CH_3O^* + H_2O + e^-$	1.10	0.48	1.20	0.61	1.23	0.60
$CH_2OH^* + OH^- \rightarrow CHOH^* + H_2O + e^-$	0.27	-0.91	0.42	-0.88	0.41	-0.86
$CH_2OH^* + OH^- \rightarrow CH_2O^* + H_2O + e^-$	0.82	-0.42	0.52	-0.30	0.55	-0.22
$CH_3O^* + OH^- \rightarrow CH_2O^* + H_2O + e^-$	0.06	-1.07	0.04	-1.12	0.07	-1.07
$CHOH^* + OH^- \rightarrow CHO^* + H_2O + e^-$	0.17	-0.64	0.17	-0.64	0.22	-0.66
$CHOH^* + OH^- \rightarrow COH^* + H_2O + e^-$	0.66	-1.06	0.46	-1.17	0.35	-1.25
$CH_2O^* + OH^- \rightarrow CHO^* + H_2O + e^-$	0.39	-1.13	0.48	-1.23	0.46	-1.29
$CHO^* + OH^- \rightarrow CO^* + H_2O + e^-$	0.41	-1.70	0.46	-1.74	0.47	-1.77
$COH^* + OH^- \rightarrow CO^* + H_2O + e^-$	0.97	-1.28	0.96	-1.22	0.86	-1.18
$CO^* + OH^- \rightarrow COOH^* + H_2O + e^-$	0.83	0.21	0.87	0.18	0.93	0.22
$COOH^* + OH^- \rightarrow CO_2 + H_2O + e^-$	/	-1.21	/	-1.13	/	-1.12

The reason why Au@PtAu-1 possesses the lowest reaction barrier for the rate-determining dehydrogenation step could be explained by analyzing the transition state. Given that the energy of transition state (CH_3OH-CH-TS) is determined by the equation (1).

$$E(\mathrm{TS}) = E(CH_2OH^*) + E(H^*) + E(\mathrm{int}) \qquad \text{Eq.(1)}$$

Where E(TS) is the chemisorption energy of transition state which can be spilt into three terms, namely, $E(CH_2OH^*)$, E(H*), and E(int), representing the chemisorption energy of CH_2OH^* at the transition state without H*, the chemisorption energy of H at the transition state geometry without CH_2OH^*, and a quantitative measurement of the interaction between CH_2OH^* and H* at the transition state, respectively. The positive value of E(int) represents a repulsive interaction while the negative values imply an attractive interaction. For the three models, the E(TS) for CH_3OH-CH-TS is mainly determined by the value of E(int). The values of E(int) for Au@PtAu-1, Au@PtAu-2 and Au@PtAu-3 are -0.05, -0.01 and 0.11 eV, respectively, indicating for Au@PtAu-1, an attractive interaction between the carbon fragment and H species exists when dehydrogenation occurs on it, suggesting Au@PtAu-1 possess the most favorable surface atomic arrangement mode for C-H cleavage with lowest reaction barrier energy.

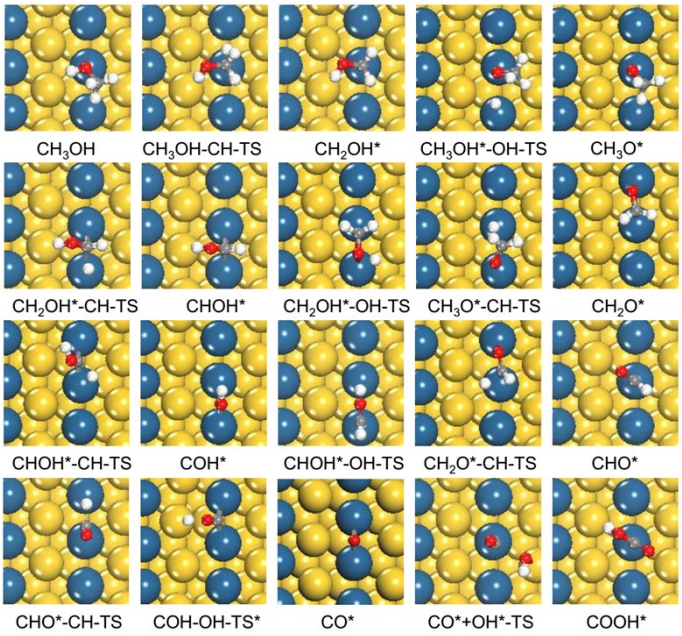

Figure S17. Optimized adsorption configurations of intermediates and TS involved in methanol oxidation on the Au@PtAu-1 surface, related to Figure 3. Yellow, blue, red, gray and white balls denote Au, Pt, O, C and H atoms, respectively. (TS refer to transition state)

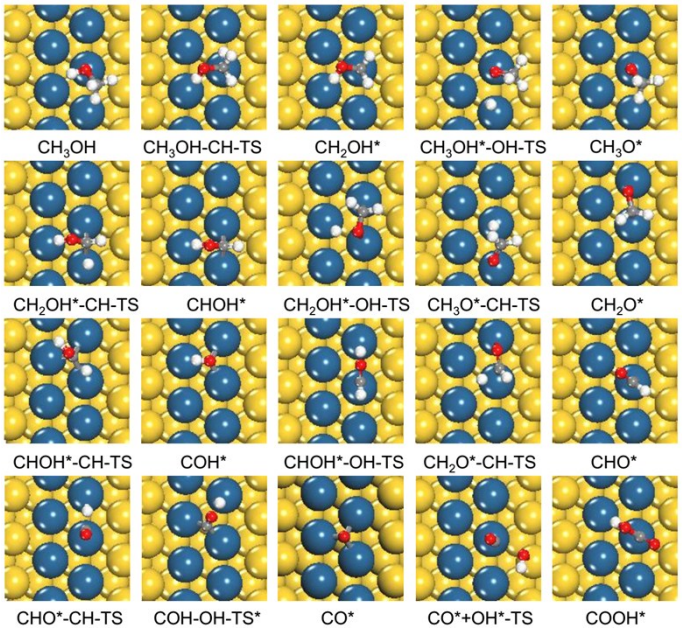

Figure S18. Optimized adsorption configurations of intermediates and TS involved in methanol oxidation on the Au@PtAu-2 surface, related to Figure 3. Yellow, blue, red, gray and white balls denote Au, Pt, O, C and H atoms, respectively. (TS refer to transition state)

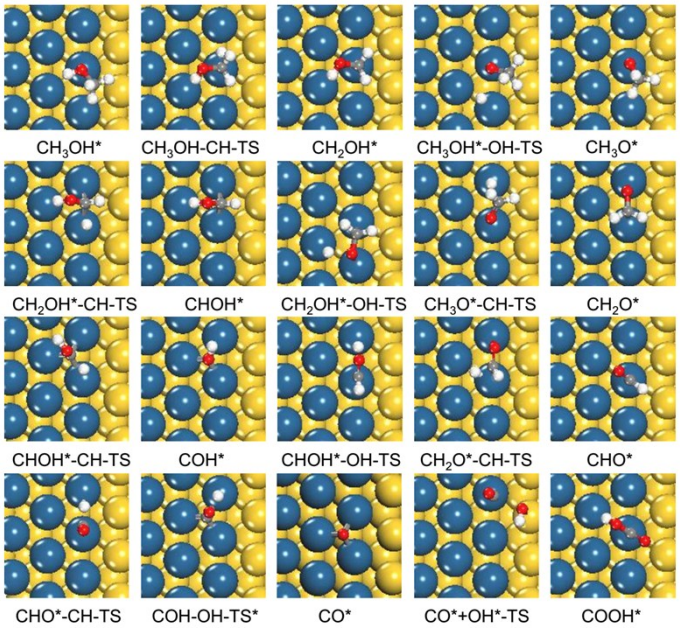

Figure S19. Optimized adsorption configurations of intermediates and TS involved in methanol oxidation on the Au@PtAu-3 surface, related to Figure 3. Yellow, blue, red, gray and white balls denote Au, Pt, O, C and H atoms, respectively. (TS refer to transition state)

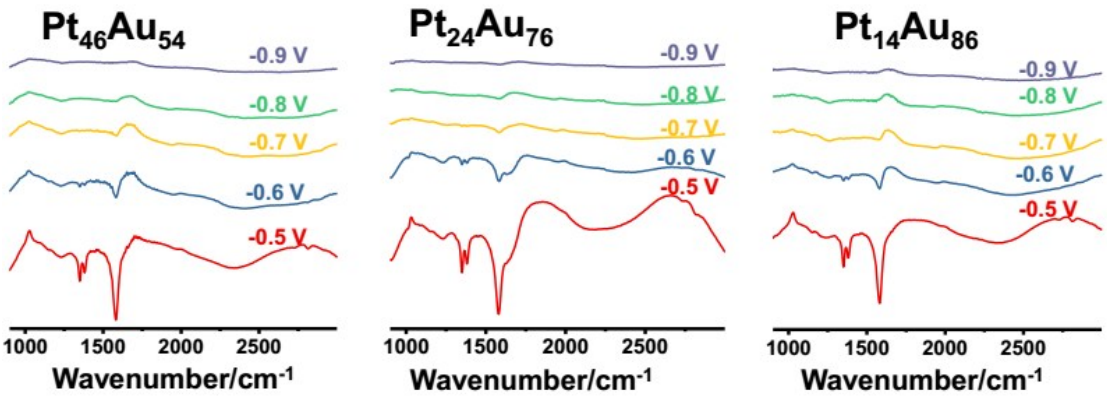

Figure S20. *In situ* FTIR spectra for methanol oxidation obtained from PtAu alloys modified electrode during a potential step experiment. Note that due to the weak intensities of CO absorption band as well as the sensitivity limitation of FTIR technique, difference of in situ FTIR spectra obtained on different PtAu alloys modified electrode hardly observed.

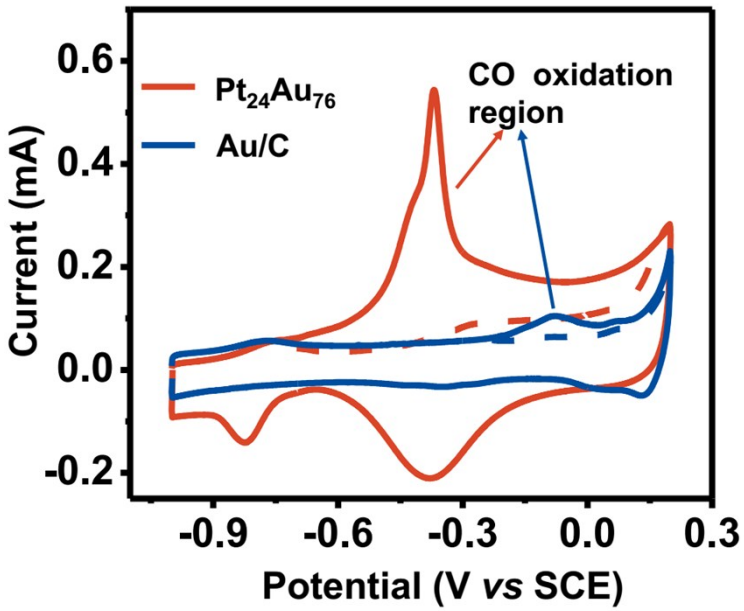

Figure S21. CO oxidation removal tests. Comparison of CO stripping voltammograms for $Pt_{24}Au_{76}$ and Au/C in 1.0 M KOH solution at a scan rate of 50 mV s^{-1}, related to Figure 4. To explore the possibility of Au being involved in CO oxidation removal given that nanosized gold has previously demonstrated to be active for CO oxidation. The CO-stripping voltammetry test for as-synthesized Au nanoparticle was further carried out and compared with that of $Pt_{24}Au_{76}$ (Figure S19). Clearly, despite a tiny CO-oxidation peak being observed for Au/C, the amount of absorbed CO on Au nanoparticles is much less than that on $Pt_{24}Au_{76}$. Besides, the onset potential for $Pt_{24}Au_{76}$ is lower than that on Au nanoparticle, which ruled out the possibility of Au being as the main catalytic sites for MOR.

Table S7. List of the onset potential (V *vs* SCE), the peak potential (V *vs* SCE) and the peak current (mA) of PtAu alloys and Pt/C obtained from Figure 4.

Catalyst	onset potential (V)	peak potential (V)	peak current (mA)
$Pt_{46}Au_{54}$	-0.73	-0.39	0.33
$Pt_{24}Au_{76}$	-0.76	-0.37	0.55
$Pt_{14}Au_{86}$	-0.73	-0.37	0.27
Pt/C	-0.57	-0.38	0.13

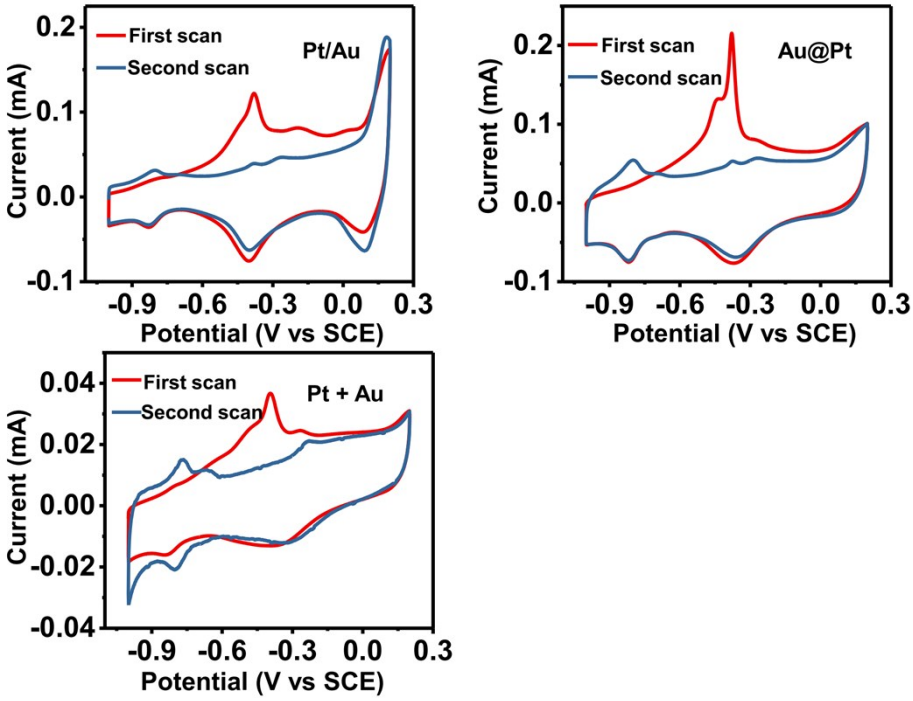

Figure S22. CO stripping voltammograms. CO stripping voltammograms for Pt/Au heterodimer (a), Au@Pt core-shell nanostructure (b) and Au + Pt (c) in 1.0 M KOH solution at a scan rate of 50 mV s^{-1}, related to Figure 4.

2 Supplemental experimental procedures

2.1 General chemicals and instrumental description

Chemicals and Materials. Chloroauric acid hydrated ($HAuCl_4 \cdot 4H_2O$), platinum(II) 2,4-pentanedionate ($Pt(acac)_2$, 98%), borane-tert-butylamine complex (TBAB), 1-octadecene (ODE, 90%), nafion solution (5 wt%), platinum on activated carbon (Pt/C, 20 wt%) were all obtained from Alfa Aesar. Tri-*n*-octylphosphine oxide (TOPO, 95%) and oleylamine (OAm, 80-90%) were purchased from Tokyo Chemical Industry and Sigma Aldrich, respectively. Cyclohexane, potassium hydroxide, ethanol, toluene, *n*-hexane, cyclohexane and isopropanol were provided by Beijing Chemical Works. Ketjen Black was purchased from Shanghai HESEN Electric Company.

Instrumental description. TEM images were obtained from a Hitachi HT7700 transmission electron

microscope at 120 kV. The HRTEM characterization was performed on a JEOL JEM-2100F transmission electron microscope (Japan) operating at 200 kV. Powder XRD patterns were recorded on a Bruker AXS D8-Advanced X-ray diffractometer (Germany) operating at 40 mA and 45 kV using monochromated Cu *K*α radiation (incident angle = 0.5°, λ = 1.5418 Å, step size = 0.5°, integration time 20 s/step). The elemental composition of the bulk of the NPs was measured by an inductively coupled plasma optical emission spectroscopy (ICP-OES, iCAP 6000 series, Thermo Scientific). The surface composition of NPs was obtained from X-ray photoelectron spectrum (XPS, ESCALAB 250).

2.2 Synthetic procedures

Synthesis of $Pt_{46}Au_{54}$, $Pt_{24}Au_{76}$ and $Pt_{14}Au_{86}$ nanoparticles (NPs). The Pt-Au alloys were prepared through thermal decomposition method in the OAm and ODE solvent system with slight variation on the amount of precursor and reducing agent. The metal precursors were prepared by utilizing tri-*n*-octylphosphine oxide (TOPO) as the capping agent for platinum (II) acetylacetonate ($Pt(acac)_2$) and chloroauric acid hydrated ($HAuCl_4 \cdot 4H_2O$) considering TOPO could effectively modulate the redox potentials of metal ions. In a typical synthesis of $Pt_{24}Au_{76}$ NPs, $Pt(acac)_2$ (9.8 mg), $HAuCl_4 \cdot 4H_2O$ (30.9 mg), TOPO (200 mg), OAm (4 mL) and ODE (6 mL) were added into a three-necked flask under magnetic stirring. N_2 was bubbled into the reactor to remove O_2 and the inert atmosphere was kept throughout the synthesis. Then the mixture solution was rapidly heated to and maintained at 260 °C for 60 min. After naturally cooling down to 80 °C, the $Pt_{24}Au_{76}$ NPs were collected by centrifugation at 10,000 rpm and washed three times with mixed solvents of cyclohexane and ethanol to remove extra capping agents. The obtained product was redispersed in 2 mL of cyclohexane for later use. Similarly, $Pt(acac)_2$ (19.7 mg), $HAuCl_4 \cdot 4H_2O$ (20.6 mg) and TOPO (200 mg) were used to prepare $Pt_{46}Au_{54}$ NPs and $Pt(acac)_2$ (6.7 mg), $HAuCl_4 \cdot 4H_2O$ (32.7 mg) and TOPO (500 mg) were used to obtain $Pt_{14}Au_{86}$ NPs, respectively.

Synthesis of Au NPs. $HAuCl_4 \cdot 4H_2O$ (30.9 mg), TOPO (200 mg), OAm (4 mL) and ODE (6 mL) were added into a three-necked flask with magnetic stirring under N_2 flow. Then the solution was heated to and maintained at 180 °C for 30 min. When naturally cooled to 80 °C, the Au NPs were collected by centrifugation at 10000 rpm and washed three times with a mixed solution of cyclohexane and ethanol to remove extra capping agent. The obtained product was redispersed in 2 mL of cyclohexane for later use.

Synthesis of Pt/Au heterodimer. Pt/Au heterodimer were prepared *via* a typical two-step synthesis process. $Pt(acac)_2$ (9.8 mg), TOPO (200 mg), OAm (4 mL) and ODE (6 mL) were added into a three-necked flask under magnetic stirring in an inert atmosphere. The mixture was heated to and maintained at 230 °C for 30 min to form homogeneous solution. Subsequently, the gold precursor, consisting of 30.9 mg of $HAuCl_4 \cdot 4H_2O$ and 1 mL of ethanol, was injected into the above resulting solution when it cooled to 80 °C naturally. By further maintaining at this temperature for another 30 min, the color of solution changed from dark black to wine red gradually. Pt/Au heterodimers were obtained by centrifugation at 8,000 rpm and washed three times with a mixture of cyclohexane and ethanol. The obtained product was redispersed in 2 mL of cyclohexane for later use.

Synthesis of Au@Pt structure. In order to prepare Au@Pt core-shell structure, a typical seeding method was adopted. 2-3 nm Au NPs were synthesized at room temperature and used as seeds for fabrication of Au@Pt core-shell structure. Specifically, $HAuCl_4 \cdot 4H_2O$ (50 mg), toluene (5 mL) and OAm (5 mL) were added into a three-necked flask with magnetic stirring under N_2 flow. After 10 minutes, TBAB (0.025 mmol) dissolved in toluene (0.5 mL) and oleylamine (0.5 mL) was added into three-necked flask, stirring for 30 min. Thereafter, the Au NPs were collected by centrifugation at 7,000 rpm using ethanol as precipitating agent and the obtained product was redispersed in 2 mL of n-hexane. In a typical synthesis of Au@Pt core-shell structure, Au NPs (3 mg) dissolved in *n*-hexane (1 mL), OAm (4 mL) and ODE (6 mL) were added into a three-necked flask with magnetic stirring under N_2 flow. The mixture was heated to and maintained at 100 °C for 15 min to allow evaporation of *n*-hexane. Then the mixture was heated up to 200 °C, further keeping at this temperature for another 30 min. And the color of the solution changed from wine red to dark black gradually. Au@Pt core-shell structures were obtained by centrifugation at 8,000 rpm and washed for three times with a mixture of cyclohexane and ethanol. The obtained product was redispersed in 2 mL of cyclohexane for later use.

Preparation of nanocrystals loaded carbon (NCs/C) catalyst ink. 4 mg of Ketjen Carbon, 6 mL of cyclohexane and 3 mg of nanocrystals were mixed in a 10 mL centrifuge tube. The mixture was sonicated to make nanocrystals completely be loaded on carbon substrate, as suggesting by the clear supernatant. The product was collected by centrifugation at 8,000 rpm and washed twice with a mixture of cyclohexane and ethanol. After mixing with 40 mL of glacial acetic acid in a 100-mL flask, the mixture was heated to and kept at 70 °C for 2 h, which was mainly utilized for removing surface ligands so as to reduce activation time during electrochemical test. [S1] The NCs/C product was obtained by centrifugation at 8,000 rpm and washed three times with ethanol to remove excess glacial acetic acid. The resulting product was dried at 60 °C in a vacuum oven. Eventually, 4 mg of NCs/C or commercial Pt/C was added in the mixture of ultrapure water, isopropanol and Nafion solution (5 wt%) (v/v/v 3:3:0.2), followed by sonication to form uniform suspension.

2.3 Electrochemical measurement setup

CV measurements of PtAu NPs surface composition. The surface composition of PtAu NPs were measured through cyclic voltammetry curves in 0.5 M H_2SO_4 solution at 50 mV/s by following previously reported methods. [2-4] The electrochemical surface areas (ESA) of Pt were gained by integrating and averaging hydrogen adsorption and desorption region [$(Q_{ads} + Q_{des})/2$], which was translated into cm^2_{Pt} by dividing with 230 $\mu C/cm^2_{Pt}$ conversion. The ESA of Au was calculated *via* integrating the capacity-corrected Au oxide formation peak area, which was converted to cm^2_{Au} by splitting with 340 mC/cm^2_{Au} conversion.

Methanol oxidation measurements. The electrochemical methanol oxidation was conducted in a three-electrode cell by electrochemical workstation (CHI 660E, CH Instrument, Inc.) at room temperature. A glassy carbon electrode (diameter: 3 mm), a saturated calomel electrode and a graphite rod were used as the working, reference and counter electrode, respectively. The loading amount of Pt on glassy carbon electrode for all the catalysts was 1.79 μg, which was determined by ICP-OES. The electrochemically active surface areas (ECSA) were measured *via* integrating the hydrogen desorption

charge on the CVs in N_2-saturated 1.0 M KOH solution at a sweep rate of 50 mV/s. CV measurements and stability test of MOR were carried out in N_2-saturated 1.0 M KOH and 1.0 M CH_3OH solution at a sweep rate of 50 mV/s. CO-stripping tests of all catalysts were conducted in 1.0 M KOH solution. The maximum coverage of CO at the Pt active sites was realized by insufflating CO gas (99.9%) for 15 min at -1.0 V (vs. SCE). Then the residual CO in the solution was removed by bubbling N_2 for 30 min.

Oxygen reduction measurements. The electrochemical oxygen reduction was conducted in a three-electrode cell by electrochemical workstation (CHI 660E, CH Instrument, Inc.) at room temperature. A rotating disk electrode (RDE) with a glassy carbon (GC) disk of 5 mm in diameter, a saturated calomel electrode and a graphite rod were used as the working, reference and counter electrode, respectively. The loading amount of Pt on glassy carbon electrode for all the catalysts was 4.77 μg determined by ICP-OES. The ECSA values were measured *via* integrating the hydrogen desorption charge on the CVs in N_2-saturated 0.1 M KOH solution. CV measurements were carried out in N_2/O_2-saturated 0.1 M KOH solution at the rate of 50 mV/s, and the linear sweep voltammetry (LSV) scans at various rotating speed were tested in N_2/O_2-saturated 0.1 M KOH at 10 mV/s.

The electron transfer number per oxygen molecule for oxygen reduction can be obtained according to Koutecky-Levich (K-L) equation. [5]

$$\frac{1}{J}=\frac{1}{J_L}+\frac{1}{J_K}=\frac{1}{B\omega^{1/2}}+\frac{1}{J_K}$$

$$B=0.62nFC_0D_0^{2/3}V^{-1/6}$$

J, J_K and J_L represent the measured current density, kinetic and diffusion limited current densities, respectively. ω is the angular velocity of the disk; n stands for the electron transfer number; F is the Faraday constant (96485 C/mol); C_0 represents the bulk concentration of O_2 (1.2×10^{-6} mol/cm^3); D_0 is the diffusion coefficient of O_2 in 0.1 M KOH (1.9×10^{-5} cm^2/s); V stands for the kinematic viscosity of electrolyte (0.01 cm^2/s).

2.4 Computational methods

All the electronic structure calculations were performed using the SIESTA package with Troullier-Martins norm conserving pseudopotentials.[6-8] The exchange-correlation functional utilized was at the generalized gradient approximation (GGA) level with Perdew-Burke-Ernzerhof (PBE).[9] A double-ξ plus polarization (DZP) basis set was employed and the orbital-confirming cutoff was determined from an energy shift of 0.01 eV. The transition states were located with a constrained optimization approach with the force converge criteria below 0.05 eV/Å.[10-12] A four-layer slab was modeled by a $p(2 \times 8)$ supercell with a three-layer Au(111) substrate and a one-layer PtAu shell. The cut-off energy for the real space grid was 250 Ry. A 2×5×1 Monkhorst-Pack *k*-point mesh was used. The vacuum region was ~12 Å to eliminate interactions between slabs. The mixed PtAu layer including 8 Pt atoms and 8 Au atoms was placed epitaxially on three-layer Au(111) substrate with different arrangements as shown in Figure 3. In the Au@PtAu-1 model, each one Pt row was surrounded by two Au rows and vice versa.

Two Pt and two Au rows were assembled in the Au@PtAu-2 model and four Pt and four Au rows were assembled in the Au@PtAu-3 model. For each adsorbate in the oxidation of methanol to CO_2, different binding sites were examined to determine the most suitable configuration.

The free energy of species was obtained from $G = E + ZPE - TS$, where E is the total energy of species, S is the entropy and ZPE is the zero point energy at room temperature (300 K). The reaction free energy of $AH \rightarrow A + H^+ + e^-$ was calculated as $\Delta G = G(A) + G(H^+ + e^-) - G(AH)$. At the electrode potential of 0 V, pH = 0 ($[H^+] = 1M$), at 298 K, due to the equilibrium of $H^+ + e^- \rightarrow \frac{1}{2} H_2$, we can use the free energy of $\frac{1}{2} H_2$ in the gas phase to replace that of $H^+ + e^-$.[13] The correction terms for pH ($-pHkT\ln 10$) and electrode potentials (eU) referring to the standard hydrogen electrode were added to shift the free energies under the realistic condition. All vibrational frequencies of adsorbates, v_i(Hz), were calculated based on the harmonic oscillators approximation. [14]

2.5 *In situ* infrared spectroscopy

Electrochemical *in situ* FTIR spectra were obtained from a Nexus 870 FTIR spectrometer (Nicolet), which is equipped with a liquid-nitrogen-cooled MCT-A detector, an EverGlo IR source and at a spectral resolution of 8 cm^{-1}. In this configuration, infrared radiation sequentially passed through a CaF_2 window and a thin-layer solution (about 10 μm), and then it was reflected by the electrode surface. The resulting spectra were reported as relative change in reflectivity:

$$\frac{\Delta R}{R} = \frac{R(E_S) - R(E_R)}{R(E_R)}$$

where $R(E_S)$ and $R(E_R)$ are the single-beam spectra collected at sample potential E_S and reference potential E_R, respectively.

To obtain the best spectroscopic results, we slightly modified the formulation of the catalyst ink. 3.0 mL of water, 3.0 mL of isopropanol and 0.2 mL of Nafion was mixed together and ultrasonicated for 30 min. Thereafter, 4 mg of catalyst powder for each samples was dispersed in 1 mL of the resulting mixture, which was immersed in an ultrasonic bath for 30 min to get a homogeneous ink. Afterwards, 10 μL of catalyst ink was drop-casted onto the GC electrode. The reference and counter electrodes were saturated calomel electrode (SCE) reference electrode and Pt foil, respectively. The electrolyte was 1.0 M KOH with 1.0 M methanol. For the *in situ* infrared measurements, the reference spectrum was collected at -1.0V V (vs. SCE), and the sample spectra were collected at different potentials (-0.9 V ~ 0.2 V) and corrected with respect to the reference spectrum.

3 Supplemental References

1. H. W. Huang, K. Li, Z. Chen, L. H. Luo, Y. Q. Gu, D. Y. Zhang, C. Ma, R. Si, J. L. Yang, Z. M. Peng and J. Zeng, *J. Am. Chem. Soc.* , 2017, **139**, 8152-8159.
2. J. Suntivich, Z. Xu, C. E. Carlton, J. Kim, B. Han, S. W. Lee, N. Bonnet, N. Marzari, L. F. Allard, H. A. Gasteiger, K. Hamad-Schifferli and Y. Shao-Horn, *J. Am. Chem. Soc.*, 2013, **135**, 7985-

7991.

3. T. Tan, H. Xie, J. Xie, H. Ping, B.-L. Su, W. Wang, H. Wang, Z. A. Munir and Z. Fu, *J. Mater. Chem. A*, 2016, **4**, 18983-18989.
4. W. Tang, S. Jayaraman, T. F. Jaramillo, G. D. Stucky and E. W. McFarland, *J. Phys. Chem. C*, 2009, **113**, 5014-5024.
5. R. Jiang, L. Li, T. Sheng, G. F. Hu, Y. G. Chen and L. Y. Wang, *J. Am. Chem. Soc.*, 2018, **140**, 11594-11598.
6. N. Troullier and J. L. Martins, *Phys. Rev. B: Condens. Matter*, 1991, **43**, 1993-2006.
7. J. Junquera, O. Paz, D. Sanchez-Portal and E. Artacho, *Phys. Rev. B: Condens. Matter*, 2001, **64**.
8. J. M. Soler, E. Artacho, J. D. Gale, A. Garcia, J. Junquera, P. Ordejon and D. Sanchez-Portal, *J. Phys.: Condens. Matter*, 2002, **14**, 2745-2779.
9. J. P. Perdew, K. Burke and M. Ernzerhof, *Phys. Rev. Lett.*, 1996, **77**, 3865-3868.
10. A. Alavi, P. Hu, T. Deutsch, Silvestrellij, P. L. Uuml and R. Hutter, *Phys. Rev. Lett.*, 1998, **80**, 3650-3653.
11. A. Michaelides, Z. P. Liu, C. J. Zhang, A. Alavi, D. A. King and P. Hu, *J. Am. Chem. Soc.* , 2003, **125**, 3704-3705.
12. Z. P. Liu and P. Hu, *J. Am. Chem. Soc.*, 2003, **125**, 1958-1967.
13. J. K. Norskov, J. Rossmeisl, A. Logadottir, L. Lindqvist, J. R. Kitchin, T. Bligaard and H. Jonsson, *J. Phys. Chem. B*, 2004, **108**, 17886-17892.
14. A. A. Gokhale, S. Kandoi, J. P. Greeley, M. Mavrikakis and J. A. Dumesic, *Chem. Eng. Sci.*, 2004, **59**, 4679-4691.